Pressure dependence of spin canting in ammonium metal formate antiferromagnets†

Ines E. Collings, *[ab] Rudra Sekhar Manna, *[cd] Alexander A. Tsirlin,*[c] Maxim Bykov, [e] Elena Bykova,[f] Michael Hanfland,[b] Philipp Gegenwart,[c] Sander van Smaalen, [a] Leonid Dubrovinsky[e] and Natalia Dubrovinskaia[a]

High-pressure single-crystal X-ray diffraction at ambient temperature and high-pressure SQUID measurements down to 2 K were performed up to ~2.5 GPa on ammonium metal formates, $[NH_4][M(HCOO)_3]$ where M = Mn^{2+}, Fe^{2+}, and Ni^{2+}, in order to correlate structural variations to magnetic behaviour. Similar structural distortions and phase transitions were observed for all compounds, although the transition pressures varied with the size of the metal cation. The antiferromagnetic ordering in $[NH_4][M(HCOO)_3]$ compounds was maintained as a function of pressure, and the magnetic ordering transition temperature changed within a few kelvins depending on the structural distortion and the metal cation involved. These compounds, in particular $[NH_4][Fe(HCOO)_3]$, showed greatest sensitivity to the degree of spin canting upon compression, clearly visible from the twenty-fold increase in the low-temperature magnetisation for $[NH_4][Fe(HCOO)_3]$ at 1.4 GPa, and the change from purely antiferromagnetic to weakly ferromagnetic ordering in $[NH_4][Mn(HCOO)_3]$ at 1 GPa. The variation in the exchange couplings and spin canting was checked with density-functional calculations that reproduce well the increase in canted moment within $[NH_4][Fe(HCOO)_3]$ upon compression, and suggest that the Dzyaloshinskii–Moriya (DM) interaction is evolving as a function of pressure. The pressure dependence of spin canting is found to be highly dependent on the metal cation, as magnetisation magnitudes did not change significantly for when M = Ni^{2+} or Mn^{2+}. These results demonstrate that the overall magnetic behaviour of each phase upon compression was not only dependent on the structural distortions but also on the electronic configuration of the metal cation.

Introduction

Magnetic metal–organic frameworks (MOFs) or coordination polymers (CPs) have attracted increasing interest due to their capabilities of coupling magnetism with other properties, such as ferroelectricity,[1–6] porosity,[7,8] and optical activity.[9,10] The high structural flexibility and responsive nature of MOFs or CPs mean that significant changes in their magnetic properties could be achieved upon their exposure to external stimuli, such as pressure, temperature, light, or upon incorporation of guest molecules.[7,9–14] For example, (i) inclusions of different guest molecules in $Fe_3(HCOO)_6$ resulted in a variation of the magnetic properties due to the changes in the host–guest interactions;[7] and (ii) a significant increase in the magnetic transition temperature could be achieved with increasing pressure in cyanide-bridged bimetallic ferrimagnets due to the reduction in the distances of the M–CN–M linkages.[12]

Design strategies for improving the magnetic properties of MOFs and CPs are important due to the large number of chemical modifications that can affect their magnetic behaviour. These include variation of the magnetic metal cation,[15–20] the ligand and its functionalisation,[21,22] as well as ions or guest atoms/molecules within the pores.[7,17,23–25] Certain guidelines, such as the Goodenough–Kanamori–Anderson rules can be used to predict whether the resulting magnetic order is

[a] Laboratory of Crystallography, University of Bayreuth, 95440 Bayreuth, Germany
[b] European Synchrotron Radiation Facility, 71 avenue des Martyrs, 38000 Grenoble, France. E-mail: ines.collings@esrf.fr
[c] Experimental Physics VI, Center for Electronic Correlations and Magnetism, Augsburg University, 86159 Augsburg, Germany. E-mail: altsirlin@gmail.com
[d] Department of Physics, IIT Tirupati, Tirupati 517506, India. E-mail: rudra.manna@iittp.ac.in
[e] Bayerisches Geoinstitut, University of Bayreuth, 95440 Bayreuth, Germany
[f] Deutsches Elektronen-Synchrotron DESY, Notkestraße 85, 22607 Hamburg, Germany

† Electronic supplementary information (ESI) available: Synthesis of AMFs, powder X-ray diffraction, ambient pressure SQUID measurements, susceptibility fits, Binder cumulant, preferred spin directions, canted moments for ANiF and AMnF, high-pressure SQUID measurements for ACoF, relations between the HP phases, twinning of AMF-III, lattice parameters and bulk moduli, H-bonding in AMF-II and AMF-III phases, and pressure dependence of octahedral angles. Crystal structures upon compression have been deposited to the CCDC with the numbers 1861329–1861359. For ESI and crystallographic data in CIF of experimental and DFT-relaxed structures or other electronic format see DOI: 10.1039/c8cp03761b

likely to be antiferromagnetic (AFM) or ferromagnetic (FM).[26–28] In particular, in order to determine the different levels of AFM and FM superexchange interactions, the following should be considered: (i) the electronic orbital configuration of the metal cations and bridging anion involved, and (ii) the metal–ligand–metal binding angle.[27] It was shown for Prussian blue compounds that decreasing the competition between AFM and FM interactions could give rise to an increase in T_N.[29] Thus the Prussian Blues with metal cations that could only exhibit AFM interactions *via* the cyanide linker gave rise to the highest magnetic transition temperature (*e.g.* $KV^{II}Cr^{III}(CN)_6{\cdot}2H_2O$, $T_N = 370$ K).[29,30] Considering ligands with multiple atoms, not only is the variation of metal–ligand–metal binding angle significant for the resulting AFM and FM interactions, but also that of the torsion angle. For example, within the families of metal azides $Ni(N_3)_2(L)$ and $Mn(N_3)_2(L)$, an important link was established between the M–ligand–M torsion angles and the resulting magnetic ordering and its transition temperature.[31,32]

The application of pressure on magnetic materials allows the study of continuous structural modifications and variations in the magnetic properties without additional electronic effects that would be present upon chemical substitutions. Many studies have shown that pressure can induce an increase in the magnetic transition temperature,[11,13,14,33–35] as is theoretically predicted from the volume dependence of superexchange.[36] The shrinkage of the superexchange pathways is in many cases the reason for the increase in T_C or T_N.[11,13,33,35] However, it has also been shown that the magnetic transition temperature can decrease with increasing pressure, which may arise from a variation in the binding angle between the metal cation and the ligand thus changing the orbital overlaps.[37] The pressure-dependent magnetic behaviour can become more complex in systems for which the magnetic exchange arises from a contribution of both FM and AFM interactions.[29,38] In these cases, FM compounds have a greater tendency for their T_C to remain unchanged or decrease with pressure, while the AFM compounds generally exhibit an increase of T_N with pressure.[12,35,38] This observation can be understood by the response of AFM interactions to both M–L–M binding angle and the M–L bond distances, whilst FM interactions are most sensitive to the M–L–M binding angle.[35]

Ammonium metal formates, as well as related metal formates ($[A][M(HCOO)_3]$) with protonated amine-templating cations on the A-site, *e.g.* $(CH_3)_2NH_2^+$, have exhibited a range of interesting physical properties upon cooling, such as ferroelectric behaviour,[15,39] magnetic ordering,[2–4,15,16,40–43] and with certain compositions, multiferroic properties.[2–6] The ferroelectric behaviour exhibited upon cooling is usually through a disorder–order transition of the A-site cation.[2,15,39] Upon further cooling to below ~35 K, their magnetic ordering arises from the interaction of magnetic spins on the metal cations *via* superexchange through the formate linker to yield antiferromagnetic order,[16,44,45] while the copper formates display low-dimensional magnetic behaviour.[42,46] The antiferromagnetic coupling is usually accompanied by a canting of the spins, driven by the antisymmetric Dzyaloshinskii–Moriya interaction (DMI),[47,48] to give rise to weak ferromagnetism.[44] The shape of the formate linker is one of the reasons for allowing the DMI as it prevents the existence of inversion symmetry between the two metal centres that are connected by the formate.[44] The interest in these materials is principally motivated by the multiple ferroic parameters that can exist. However, while the ferroelectric behaviour can be achieved to near room-temperature,[3,49] the magnetic ordering remains very low, and it is not clear how the T_N values can be increased.

Here we investigate the magnetically-ordered ammonium metal formates as a function of pressure at low temperature to understand how their magnetic properties can be modified and perhaps improved. We characterise both the structural and magnetic property evolutions of ammonium metal formates, abbreviated here to AMF, where M is Mn^{2+}, Fe^{2+}, and Ni^{2+}, upon compression using single-crystal X-ray diffraction (at ambient temperature) and magnetisation measurements (down to 2 K). The structural evolutions of the AMFs with pressure show that they distort in a similar fashion within each pressure-induced phase. We determine the pressure-dependent T_N values and spontaneous magnetisation magnitudes for the AMFs and find contrasting magnetic behaviours within each phase of the different compounds. The $[NH_4][Fe(HCOO)_3]$ (AFeF) compound exhibits the greatest pressure sensitivity with respect to its magnetic properties, displaying an order of magnitude enhancement of the low-temperature magnetisation at 1 GPa. DFT calculations were performed on relaxed structures upon compression in order to validate and further understand the pressure-dependent magnetisation data. We discuss these results in terms of the spin canting amplitude, which can be related to changes in the Dzyaloshinskii–Moriya interaction, and show that the canting is sensitive to pressure but that the rate of pressure-induced change is dependent on the metal cation of the ammonium metal formate compounds.

Results

Ambient pressure structural and magnetic description

Ammonium metal formates are composed of octahedral M^{2+} cations that coordinate to formate linkers forming a three-dimensional anionic network. The $[M(HCOO)_3]^-$ network is charge balanced by ammonium cations that are located within the *c*-axis channels, and interact with the host framework *via* weak hydrogen bonding.[15] A disorder–order transition of the ammonium cations is observed in AMnF, AFeF, and ACoF upon cooling to below 254 K, 212 K, and 191 K, respectively, leading to the transformation of the ambient structure (*e.g.* $P6_322$, $a = b = 7.3236(2)$ Å, $c = 8.3180(4)$ Å for AFeF at 290 K) to a threefold superstructure (*e.g.* $P6_3$, $a = b = 12.6167(3)$ Å, $c = 8.3647(2)$ Å at 110 K for AFeF) with polar ordering of the ammonium cations.[15] In contrast, the ANiF crystal symmetry (*e.g.* $P6_322$, $a = b = 7.2861(13)$ Å, $c = 8.0207(16)$ Å at 293 K)[15] does not change upon cooling and a static disorder arrangement of the ammonium cations is observed at low temperature [Fig. 1].[16,50] Variable-temperature neutron powder diffraction measured on deuterated AMnF, AFeF, ACoF, and ANiF showed

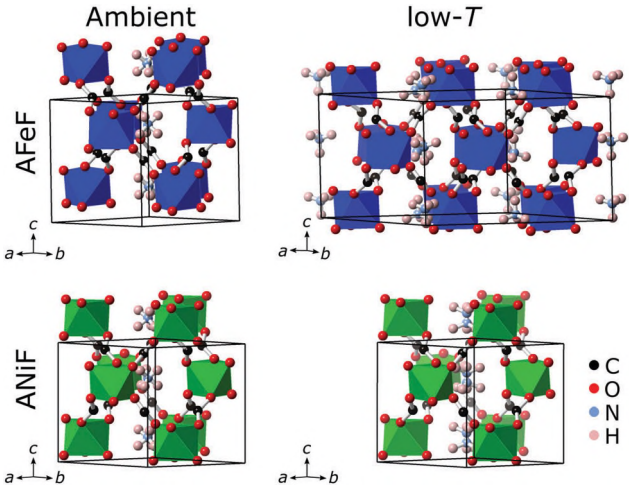

Fig. 1 Ambient pressure structures of AFeF and ANiF at ambient (293 K) and low temperature (~110 K) from ref. 15 and 50. The FeO_6 and NiO_6 coordination spheres are represented as octahedra, O atoms are in red, C in black, N in blue, and H in pink.

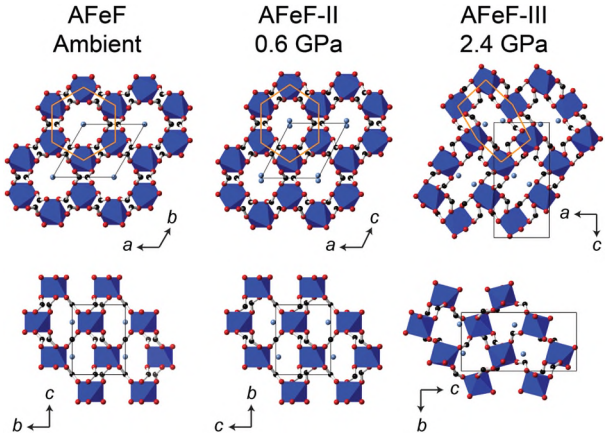

Fig. 2 Ambient and high-pressure phases of AFeF viewed down the *c*-axis and equivalent *b*-axis for the I and II/III phases (top structures), respectively, and down the *a*-axis for the structures shown below. FeO_6 octahedra are represented by blue polyhedra. Hydrogen atoms have been omitted for clarity. Hexagons are shown (in orange) to accentuate the changes in metal formate geometry in the different phases.

that the $P6_3$ (for Mn, Fe, and Co) and $P6_322$ symmetries (for Ni) are retained down to their magnetic ordering temperatures.[16] The spin directions in the antiferromagnetic structures were refined to be along the *c*-axis for the AFeF and ANiF compounds (with the $P6_3'$ and $P6_3'22'$ magnetic space groups, respectively), and in the *ab*-plane for AMnF and ACoF (with the $P2_1$ or $P2_1'$ magnetic space groups).[16] The degree of spin canting could not be detected from these measurements due to its low value (less than 1°).[16,40] The switch in spin direction across the AMF series has also been observed in $[(CH_3)_2NH_2][M^{II}Fe^{III}(HCOO)_6]$ compounds upon change in the M^{II} cations (Mn^{2+} and Co^{2+} prefer the *ab*-plane, and Fe^{2+} the *c*-axis),[51] and is related to the change in direction of the anisotropy easy axis for the different M^{2+} cations.[51]

High-pressure diffraction

High-pressure (HP) single-crystal X-ray diffraction measurements at ambient temperature showed the occurrence of two phase transitions for AMnF and AFeF, and one transition for ANiF up to 2.5 GPa (with no further transition observed up to 3.7 GPa for AFeF and ANiF from previous Raman studies).[50] The first transition from the hexagonal (termed AMF-I) to monoclinic (termed AMF-II) phases (*e.g.* $P2_1$, a = 6.8121(17) Å, b = 8.3238(9) Å, c = 7.3916(17) Å, β = 117.39(3)° for AFeF-II at 0.6 GPa) has been previously reported for AFeF, ANiF, and AZnF.[50] The second transition observed for AMnF and AFeF (second high-pressure phase termed as AMF-III) involves a doubling of the unit cell with the cell parameters as a = 6.5890(12) Å, b = 7.004(2) Å, c = 13.771(6) Å, β = 90.00(2)° for AFeF-III at 2.4 GPa [Fig. 2]. The relationship between the different unit cells of each phase are given in ESI.† The transition pressures for AMF compounds are observed at 0.31(6) and 1.17(6) GPa for AMnF-I to AMnF-II and for AMnF-II to AMnF-III, respectively; 0.50(7) and 1.95(14) GPa for AFeF-I to AFeF-II and for AFeF-II to AFeF-III, respectively; and 1.40(11) GPa for ANiF-I to ANiF-II. The errors in the transition pressures represent the pressure step between the previous phase and the transformed HP-phase. Tables S3–S5 (ESI†) give the unit cells of the AMF phases as a function of pressure. We note the phase behaviour at high pressure and low temperature may be slightly different, in particular for the transition pressures. However, as cooling mainly affects the dynamic disorder of the ammonium cation, we can assume that the main structural deformations of the framework induced by pressure can be used as a basis to understand the low-temperature magnetisation data at the same pressures.

A steady compression of AMF samples gave rise to pressure regions that contained phase mixtures, which could also be dependent on the amount of radiation received. In some cases, exposure of a fresh part of the crystal to the X-ray beam could yield a phase pure diffraction pattern, while the part of the crystal which had been exposed to the beam would remain as a phase mixture. Upon a step-wise compression of AMF single crystals, a phase mixture of AMnF-I/AMnF-II and AFeF-I/AFeF-II was observed for a further ~0.3 GPa increase after the transition pressure, while phase mixtures of AMnF-II/AMnF-III and AFeF-II/AFeF-III persisted from the transition point up to 2.5 GPa (final pressure). ANiF-I/ANiF-II phase mixtures were also present for a large pressure range, from the transition point till 2.2 GPa (final pressure). The longer phase coexistence at higher pressures could be due to the longer exposure of the crystal to the X-ray beam. Phase pure crystals of AMnF-III and AFeF-III (measured at DESY) were obtained by compressing fresh crystals directly to 1.4 GPa and 2.8 GPa, respectively.

The pressure dependence of the lattice parameters for AMnF, AFeF, and ANiF are shown in Fig. 3. From these variations, it can be seen that all structures exhibit similar anisotropic lattice parameter variation within each of their phases, however the onset of the phase transitions varies in accordance to metal cation size from Mn < Fe < Ni, where AMnF exhibits its transitions at lowest pressures, and ANiF at higher pressure. Also to note, that while both AMnF and AFeF transform into a second, much

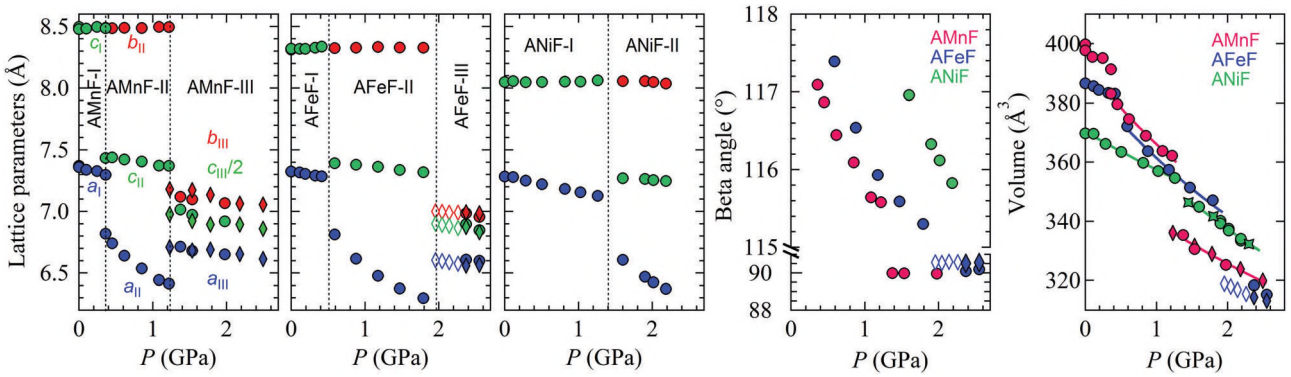

Fig. 3 Pressure dependence of the unit cell parameters of AMnF, AFeF, and ANiF with the different phases indicated by the dotted lines. In the AMnF-III and AFeF-III phases, the *c*-axis was halved, as well as the volume in order to be comparable to the other phases. On the right, the pressure dependence of the volumes of AMnF, AFeF, and ANiF (pink, blue, and green circles, respectively) are shown, with the solid lines representing the Birch–Murnaghan second-order equations of state fits (bulk moduli from these fits are given in Table S6, ESI†). The diamond markers represent unit cell parameters determined from Pawley refinements of the extracted powder diffraction from the wide image scans (±20° rotation in 2 s exposure) and the open markers in the AFeF-III phase indicate points taken upon decompression. The star markers for ANiF-II represent data from ref. 50.

denser HP-phase, ANiF remains in the first HP-phase in the pressure range studied. This could be due to the smaller size of the Ni^{2+} cation compared to Mn^{2+} and Fe^{2+}.[52] The densification which occurs upon the transition to AMnF-III and AFeF-III is due to a contraction of the framework along the *b*-axis, which does not contain any hydrogen bonding along it, thus making this axis more susceptible to large deformation [Fig. S25, ESI†]. Due to the rich structural diversity upon application of pressure within a small range, AMF compounds were ideally suited for studying the effect of these high-pressure phase transformations on their magnetic properties.

Variable-pressure magnetisation measurements

Fig. 4 shows the magnetisations as a function of pressure in the temperature range of 2–20 K (for AMnF and AFeF) and 7–40 K (for ANiF), up to 1.84 GPa (for AMnF), 1.97 GPa (for ANiF), and 2.46 GPa (for AFeF). Pressure-dependent magnetisation measurements were also performed on $[NH_4][Co(HCOO)_3]$ (ACoF), but due to the presence of a spike in the magnetisation data, which could originate from a spin-reorientation transition,[40] the data are only shown as ESI.† We note that a small peak appears in the low-temperature magnetisation data of AFeF after 1.86 GPa, which could also be due to a spin reorientation process, however further investigations would be needed to confirm this. The pressure dependence of the low-temperature spontaneous magnetisation value and the Néel temperatures (T_N) for the three ammonium metal formates are given in Fig. 5. The magnitude of spin canting was estimated using the spontaneous magnetisation value at 2 K (M_{2K}), or 7 K in the case of

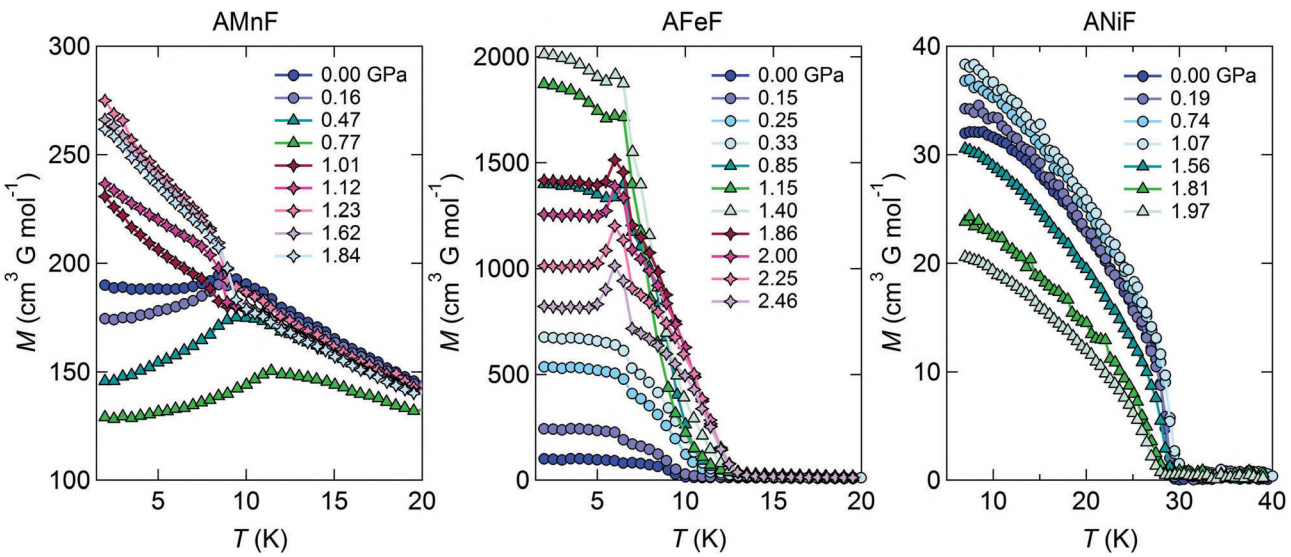

Fig. 4 Pressure dependence of the magnetisation (*M*) of AMnF, AFeF, and ANiF measured using a field of 1000 Oe for AMnF, and 100 Oe for AFeF and ANiF. The pressure points of 0.33 and 0.15 GPa for AFeF represents magnetisation measurements performed upon decompression from 2.46 GPa. The colouring and the type of symbols is related to the phase expected from diffraction, where blue circles are phase-I, green triangles phase-II, and pink/purple diamonds phase-III.

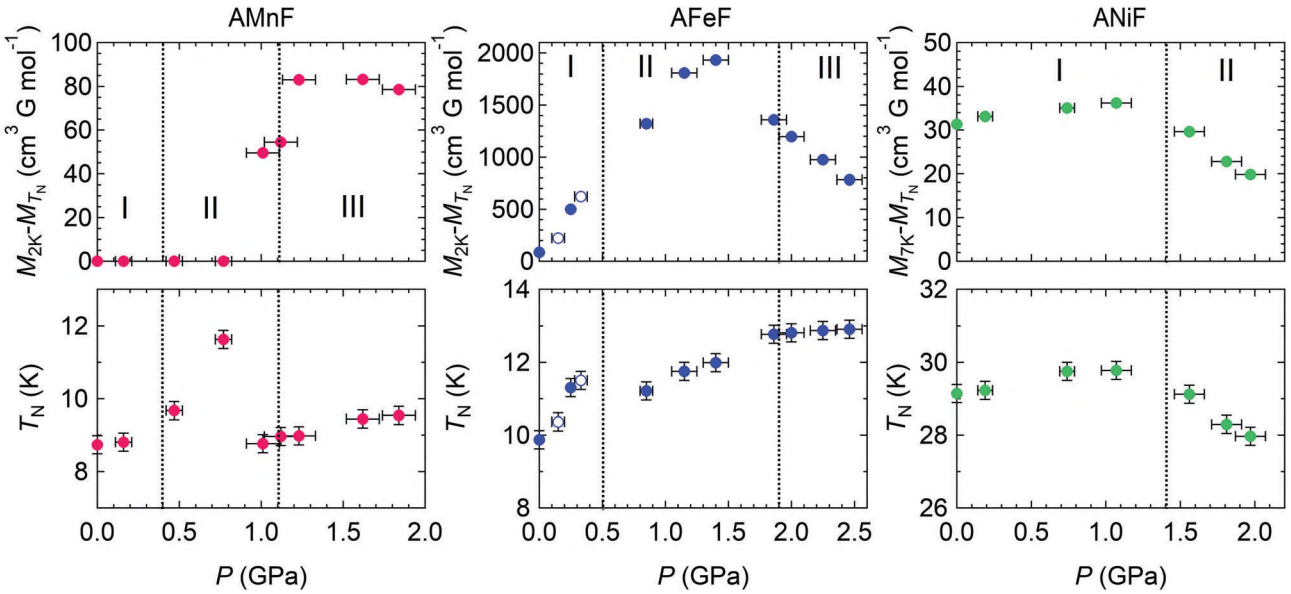

Fig. 5 Pressure dependence of the spontaneous magnetisation (M_{2K}–M_{T_N} for AMnF, AFeF or M_{7K}–M_{T_N} for ANiF) and the magnetic transition temperature (T_N) shown for AMnF (pink circles, left graphs), AFeF (blue circles, middle graphs), and ANiF (green circle; right graphs). The structural transitions (within its errors) for each compound are indicated by vertical dotted lines and the structural phase types are indicated (I to III). Values obtained upon decompression for AFeF are shown by open blue circles.

ANiF, by M_{2K}–M_{T_N} for a weakly ferromagnetic behaviour ($M_{2K} > M_{T_N}$), while for a regular antiferromagnet ($M_{2K} < M_{T_N}$), the spin canting is zero, as observed for AMnF at 0–0.77 GPa, and thus the spontaneous magnetisation value is given as zero for these regions. The magnetic transition temperature was determined from the intercept of two straight line fits to the magnetisation curve just before and after the temperature point which exhibits an abrupt change in slope. While this determination may slightly overestimate T_N by ~0.5 K, it could be easily applied to all pressure points, providing the same T_N determination method for all data. In both the AFeF and ANiF compounds, we observe an increase in magnetisation with pressure, although there is a large difference in the rate of increase: a twenty-fold enhancement is observed for AFeF between ambient pressure and 1.4 GPa, while a 1.2 times increase is seen from ambient pressure to 1.1 GPa for ANiF. These variations in the magnetisation suggest an increase in the spin canting angle, which is also clearly observed in the pressure dependence of AMnF from 0.77 to 1 GPa. In this pressure regime, there is a switch from purely antiferromagnetic to weakly ferromagnetic response, which is maintained up to the final pressure of 1.84 GPa [Fig. 4]. The variation in the spin canting for the AMnF with increasing pressure above 1 GPa is within the same magnitude as is observed for ANiF [Fig. 5].

Considering the pressure dependence of T_N, we do not observe significant variations in this parameter for all three ammonium metal formates [Fig. 5]. The T_N values are increased from ambient pressure by up to ~3 K for AFeF (at 2.46 GPa) and AMnF (at 0.77 GPa). For ANiF and AMnF, the Néel temperature decreases at $1.1 < p \leq 1.6$ GPa (by 0.7 K) and at $0.8 < p \leq 1.0$ GPa (by 2.9 K) that coincides with the ANiF-I to ANiF-II and AMnF-II to AMnF-III transitions (within the error bars of the pressure determination), respectively. For AFeF, taking into account all the data, T_N increases with a rate of 1.1 K GPa^{-1}, which is a similar pressure dependence to what was predicted for $[(CH_3)_2NH_2][Mn(HCOO)_3]$ based upon thermal expansion and specific heat measurements.[53,54] AMnF-I and AMnF-II phases show a higher T_N variation of 3.8 K GPa^{-1}, while the AMnF-III phase exhibits a rate of 0.9 K GPa^{-1}. ANiF-I displays a T_N rate of 0.7 K GPa^{-1} and the ANiF-II (as well as the ACoF-II phase, see Fig. S22, ESI†) are the only phases of the AMF family to exhibit a decrease in T_N (by −2.8 K GPa^{-1} for ANiF-II). Density functional calculations, presented in the following section, provide reasoning behind the differing pressure dependent T_N values within each phase.

The occurrence of phase transitions upon compression does affect the spin canting and magnetic transition temperatures in the AMF compounds, but in a rather unsystematic way. The spin canting in AFeF-I and AFeF-II phases are observed to increase linearly with pressure, while a decrease in canting is observed upon the transition from ANiF-I to ANiF-II that continues to decrease with pressure, and no changes are seen for the spin canting of AMnF-I through the transition to AMnF-II. The phase transition of AMF-II to AMF-III also affects the canting in a different manner: for the AFeF-II to AFeF-III transition, the canting is reduced and continues to decrease with increasing pressure, while the AMnF-II to AMnF-III transition induces spin canting, when none was observed in AMnF-I and AMnF-II phases. The magnetic transition temperature shows greater sensitivity to the structural phase transitions through changes in the slope of the T_N pressure dependence. The phases which allow the greatest pressure dependence of T_N are in the order of: AMnF-II > AFeF-I ≫ AFeF-II > AMnF-III > ANiF-I > AMnF-I > AFeF-III. Thus a certain type of structure does not always impose the same pressure dependence, and the nature of the magnetic ion seems

to play an important role, which will be discussed in greater detail in the following sections.

DFT calculations

Density functional theory calculations were performed on relaxed structures (keeping the unit cell parameters fixed) of the experimentally determined atomic positions at different pressures in order to evaluate the microscopic magnetic parameters. Exchange couplings at ambient pressure were first determined from fits to the experimental susceptibility with the model curves for cubic antiferromagnets [Fig. S15–S17, ESI†]. The resulting J values (J = 0.64 K for AMnF, J = 1.25 K for AFeF, and J = 10.6 K for ANiF) were cross-checked by calculating Néel temperatures *via* Binder cumulant for the staggered magnetisation,[55] giving 7.9 K (T_N/J = 12.3) for Mn, 10.5 K (T_N/J = 8.45) for Fe, and 28.9 K (T_N/J = 2.73) for Ni, in reasonable agreement with the experimental values of 8.9 K, 10.0 K, and 29.3 K, respectively [Fig. S18, ESI†]. The on-site Coulomb repulsion parameter U_d of DFT+U was then chosen in such a way that the J value at ambient pressure matched experimental estimates based on the fits to the magnetic susceptibility and the Néel temperature. We thus determined U_{Mn} = 5.5 eV, U_{Fe} = 8 eV, and U_{Ni} = 6.5 eV, which were further used for all pressures.

Exchange couplings were determined as the energy difference between the ferromagnetic state (E_{FM}) and the antiferromagnetic state (E_{AFM}) with antiparallel spins on nearest neighbours as $J = -(E_{AFM} - E_{FM})/(3 \times 4S^2)$, where the factor of 3 is the number of exchange bonds per metal site and S is the spin value. This yields the unique nearest-neighbour coupling J in the ambient-pressure hexagonal phases, as well as the average nearest-neighbour coupling $\bar{J}$ in the high-pressure monoclinic phases. The J values are given in Fig. 6 and show varying pressure dependence that is related to the metal cation. For the AMnF compound, the J values tend to increase with pressure, in the AFeF compound the J values are nearly constant with pressure, while for ANiF there is a decrease in J with pressure. The resulting T_N values are dependent on the magnitude of J, resulting from differing levels of AFM and FM contributions, but also on the magnetic anisotropy, where greater anisotropy tends to constrain the spins, thus assisting magnetic ordering and enhancing T_N values.

Cumulative magnetic anisotropy (E_A) was evaluated by comparing energies of spin configurations with magnetic moments directed along different crystallographic axes. The energy difference between easy and hard directions was calculated and normalized per magnetic atom. The easy-axis for the different phases is given in Table S2 (ESI†). The values of E_A are a magnitude larger for AFeF compared to AMnF and ANiF, and their pressure dependence is shown in Fig. 6. The variation in the experimental T_N pressure dependence within each phase observed in Fig. 5 can be explained by the different AFM and FM competing contributions within each phase but also from the magnetic anisotropy which varies with the metal cation.

To gain further insight into the ground-state spin configuration and the possibility of spin canting, we performed non-collinear calculations using crystallographic directions as initial spin directions. The spins were allowed to relax during the calculation, thus producing the ground-state configuration with canted spins. All cantings were compatible with crystallographic symmetries. Experimentally, spin canting can be detected as the remnant magnetisation in the field applied along the canting direction using the following equation

$$\mu = \frac{MM_u/m}{\mu_B N_A}, \quad (1)$$

where M is the measured magnetic moment (units emu), M_u the molar mass, m the sample mass, μ_B the Bohr magneton constant,

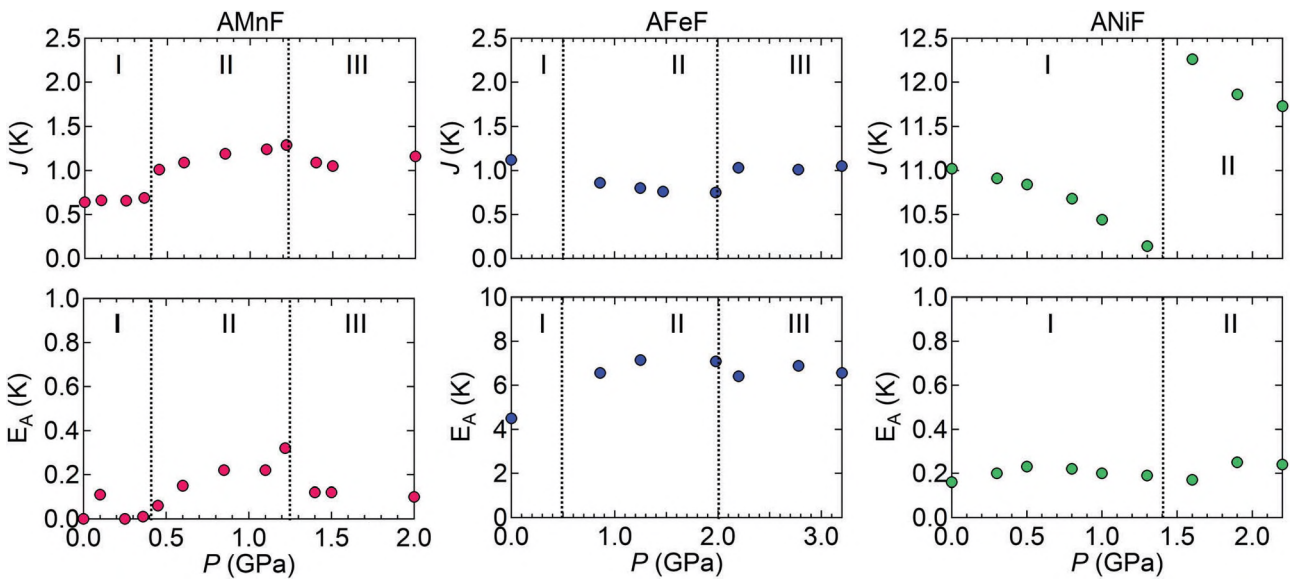

Fig. 6 Pressure dependence of DFT calculated J values or average $\bar{J}$ for the monoclinic phases, and cumulative magnetic anisotropy energy (E_A) per metal cation for AMnF (pink circles, left graphs), AFeF (blue circles, middle graphs), and ANiF (green circle; right graphs). The structural transitions (within its errors) for each compound are indicated by vertical dotted lines and the structural phase types are indicated (I to III).

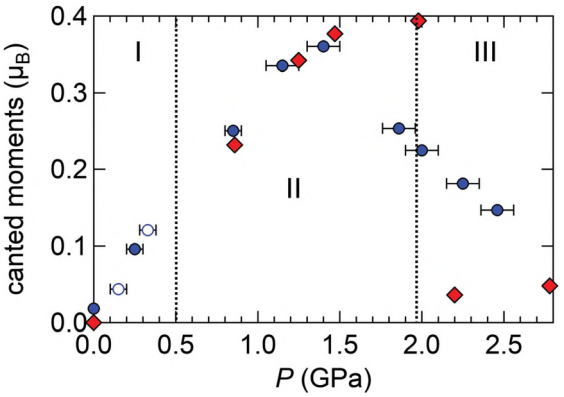

Fig. 7 The pressure dependence of the experimentally-determined maximum canted moments for three phases of AFeF (*i.e.* without powder averaging) in solid blue circles, and upon decompression in open blue circles. The diamond red symbols represent the canted moments calculated from the DFT-relaxed structures. Note that the calculated canted moment at 1.98 GPa used the AFeF-II structure type.

and N_A Avogadro's number, and were compared with the ones obtained from DFT [Fig. 7]. As the field direction is random in a powder sample, experimental remnant magnetisation measured on a powder is a third of the canted moment. The good agreement between the experimentally-determined canted moments of AFeF and those calculated from DFT calculations suggests that the origin of spin canting is due to structural and electronic effects of AFeF. Although, there is a greater difference between observed and calculated canted moments for the AFeF-I and AFeF-III phases. In the case of AFeF-III, a coexistence of AFeF-II and AFeF-III phases during the magnetisation measurements could explain the higher values of experimentally-determined canted moments compared the DFT-calculated ones, as the former would give rise to an average of both AFeF-II and AFeF-III canted moments. The phase mixture could arise from reduction in hydrostaticity and grain boundary effects between the crystallites. In the case of AFeF-I, the magnetic space group symmetry corresponds to a direct cancelling of the spin canting (as for ANiF),[16] thus a canted moment of zero is expected. However, previous magnetisation data[15,40] as well as our data clearly show the presence of a residual moment in the magnetically-ordered phase, which increases upon compression [Fig. 5]. The origin of this residual moment is not understood, but has also been observed in other systems[56] and could arise from lower-symmetry domains that average out into the known low-temperature structures, but for which a residual spin canting exists from summation over the domains. Further investigation would be needed to ascertain this possibility. The DFT calculations did not take into account lower-symmetry domains and thus give a resulting canted moment of zero per unit cell for all AFeF-I structures.

Discussion

Magnetic behaviour of the compounds in question can be described by a spin Hamiltonian

$$H = \sum_{\langle ij \rangle} J_{ij} \mathbf{S}_i \cdot \mathbf{S}_j + \sum_{\langle ij \rangle} \mathbf{D}(\mathbf{S}_i \times \mathbf{S}_j) + \sum_i A(S_i^z)^2, \qquad (2)$$

where the summation is over lattice sites i and bonds $\langle ij \rangle$, J is the Heisenberg coupling constant, $\mathbf{S}$ the spin vector, $\mathbf{D}$ the Dzyaloshinskii–Moriya vector, and A the single-ion anisotropy. The first term defines the overall energy scale. The second and third terms are typically much smaller in magnitude, but determine preferred spin direction. Additionally, the DM term is responsible for spin canting, because it favours the alignment of neighbouring spins at 90° to each other, and thus tends to create deviations from collinear spin arrangements.[47,48] As we observe only small changes in T_N, which would influence the J value, we can expect that the large changes in the low-temperature magnetisation magnitudes seen in AFeF and upon the AMnF-II to AMnF-III transition are due to the increased Dzyaloshinskii–Moriya interaction (DMI) (the second term in eqn (2)).

In the ammonium metal formates, distortions along the M–formate–M linkages could lead to the increase in DMI [Fig. 8]. Although from the high-pressure magnetisation measurements, it is clear that the spin canting in AFeF is much more susceptible to changes in pressure than ANiF or AMnF. The large enhancement of magnetisation observed in AFeF, however, cannot be allocated to a particular structural change, as the structural distortions and crystal phases observed in AFeF are similar to those in AMnF and ANiF [Fig. 3 and 8]. In order to understand the low-temperature magnetisation increase, the anisotropy parameters need to be determined, however these are much weaker and thus more difficult to track. Here, we restrict ourselves to only two parameters, the cumulative anisotropy E_A that determines preferred spin direction and the spin canting related to the antisymmetric DMI. Both parameters are quite high in AFeF and much lower in AMnF and ANiF [see Fig. S19 and S20, ESI† for the calculated canted moments of ANiF and AMnF, respectively]. This difference can be traced back to the electronic configurations, namely, the half-filled d-shell in Mn^{2+} (d^5) and the half-filled e_g shell in Ni^{2+} (d^8), compared to the more than half-filled t_{2g} shell in Fe^{2+} (d^6). The latter electronic configuration gives rise to an unquenched orbital moment in the ideal octahedral environment and should amplify anisotropy terms, as we indeed observe.

Our observation is also in agreement with a theoretical study on perovskite transition metal oxides that showed that the DM vector direction and strength could vary depending on the transition metal orbital symmetry (*i.e.* half-filled d-shells *versus* more or less than half filled).[57] Moreover, the DMI for the magnetic ions with an unquenched orbital moment (more or less than half filled d-orbitals) were much more dependent on structural distortions.[57] This means that the DMI is not readily affected by structural distortions when originating from metal cations such as Mn^{2+} and Ni^{2+} with isotropic orbital symmetries. This theory can explain the very small variations in the magnetisation magnitude for the weakly ferromagnetic ANiF-I, ANiF-II, and AMnF-III phases as a function of pressure [Fig. 5], even with the similar increases in structural distortions as observed for AFeF [Fig. 8].

The small changes of T_N (and calculated J values) with pressure could be due to the changes in both the M–M distances

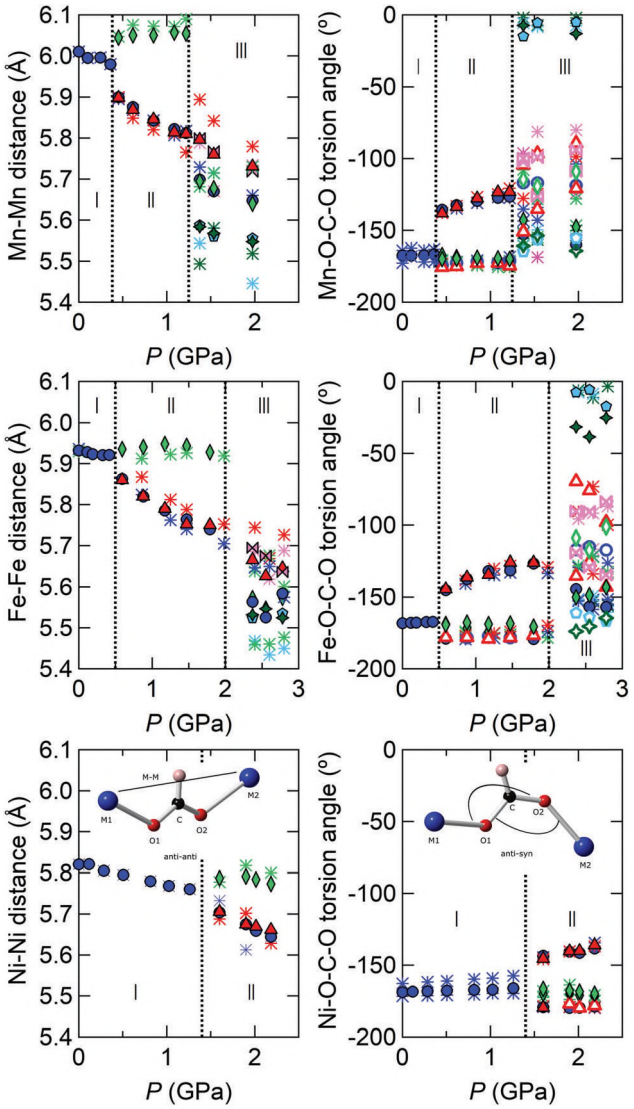

Fig. 8 The pressure dependence of the crystallographically unique metal–metal distances (connected *via* formate anions) and the M–O–C–O torsion angles for AMnF (top), AFeF (middle), and ANiF (bottom) calculated from the experimentally-determined crystal structures upon compression at ambient temperature. The different coloured symbols represent the unique M–M distance vectors and corresponding M–O–C–O torsion angles (for which there is one, three, and six for the I, II, and III phases, respectively). The M_1–O–C–O and O–C–O–M_2 torsion angles belonging to the same M_1–formate–M_2 linker are given in the same coloured symbols. Positive torsion angles are given in open symbols. The parameters obtained from DFT-relaxed structures are given in the star symbols.

and the M–formate–M binding geometries [Fig. 8], leading to two structural changes that can modify the orbital overlaps between the metal cation and the formate linker in contrasting ways.[12,36] In particular, two main types of orbital overlap combinations could allow for antiferromagnetic exchange: (i) the d_{z^2} or $d_{x^2-y^2}$ (e_g) orbitals from each metal cation mixing with the p(σ) orbitals of the oxygen from the formate, and (ii) the d_{xy}, d_{xz}, d_{yz} (t_{2g}) orbitals with the p(π) orbitals of the oxygen from the formate. The first type can have much greater orbital overlap within certain binding geometries giving rise to the stronger interaction, however, while the second type has weaker orbital overlap, it is not so dependent on the geometry of the M–formate–M binding. While reductions in the M–M distances leads to an increased orbital overlap for both e_g–p(σ) and t_{2g}–p(π) interactions,[36] distortion in the geometry of the M–formate–M links (torsion angles evolving away from 180°) would induce a worse orbital overlap for the e_g–p(σ) interactions.[58] Indeed, within the AMF-III phases, at least two out of the six unique M–formate–M links display *syn–anti* configuration (where the torsion angle of M_1–O–C–O is close to 0° while the O–C–O–M_2 angle is near 180°), instead of the purely *anti–anti* configuration (both torsion angles are close to 180°) observed in the AMF-I phase. Upon compression both the M–M distances and the M–O–C–O torsion angles reduce on average [Fig. 8], thus affecting orbital overlap in contrasting ways. The electronic configuration of the Ni^{2+} can only allow for the first type of orbital overlap for antiferromagnetic exchange, while the Mn^{2+} and Fe^{2+} can have both, although the number of possible pathways for the interaction with the p(π) orbitals of the formate decrease as the t_{2g} orbitals fill up. The changes in possible superexchange pathways are also evidenced in the different pressure dependence of J for the different AMFs [Fig. 6]. ANiF features the largest J but also shows the reduction in J upon compression (only e_g–p(σ) interactions present). AMnF reveals the opposite trend of increasing J under pressure, whereas AFeF lies between the two, with only a weak and unsystematic pressure dependence of J.

Conclusions

High-pressure experiments were used to investigate both the structural and magnetic properties of ammonium metal formates for metal cations Mn^{2+}, Fe^{2+}, Ni^{2+}. The structural data have shown the occurrence of two phase transitions for AMnF and AFeF, and one phase transition for ANiF upon compression. The magnetic behaviour of AMFs display discontinuities in the low-temperature magnetisation magnitude and the magnetic ordering temperature due to the structural transitions. The magnetic behaviour within each phase of AMFs could not be correlated despite the similar structural changes within each phase, highlighting that both structural distortions and electronic configuration of the metal cation determine the magnetic behaviour. In particular, AFeF displayed a large enhancement of magnetisation, up to 20 times at 1.4 GPa, that can be related to an increase in spin canting. This is observed in AFeF due to its sizeable magnetic anisotropy, which we ascribe to the incomplete quenching of the Fe^{2+} orbital moment, allowing the Dzyalonshinkii–Moryia interaction to be stronger and more susceptible to structural distortions. By contrast, magnetic anisotropies of AMnF and ANiF are weak, resulting in only a weak spin canting, as expected for a complete quenching of the orbital moment in Mn^{2+} and Ni^{2+}.

Isotropic exchange couplings are also influenced by the electronic configurations. A stronger coupling is found in ANiF, where only e_g orbitals are magnetic, whereas AFeF and AMnF reveal weaker couplings since both t_{2g} and e_g orbitals are active and potentially interfere. Néel temperatures show a relatively

weak pressure dependence that can be understood by simultaneous changes in the magnetic anisotropy and exchange couplings, the latter resulting from distortions in the M–formate–M exchange pathways (*e.g.* reductions in M–M distances and M–O–C–O torsion angles).

This work highlights that increase in the DMI depends both on the structural distortions and the orbital configuration of the metal cation. It suggests that large variations in spin canting could be achieved upon application of external stimuli or chemical modifications within weakly ferromagnetic materials that contain metal cations with unquenched orbital momenta.

Experimental

Ambient pressure powder diffraction

Powder diffraction was measured on the samples at ambient temperature prior to the SQUID measurements in order to confirm the purity of the samples. In the case of AFeF, two different samples were synthesised, and a small amount of iron formate dihydrate impurity (between 5–12%) was formed in both samples [Fig. S1 and S2, ESI†], however high-resolution powder X-ray diffraction on the same sample of AFeF, measured at 20 K, did not show any impurity peaks [Fig. S6, ESI†]. This could be due to the sample being better confined from moisture due to its storage in the glovebox prior to the experiment and loading within a capillary compared to the diffraction performed previously on a flat plate geometry (with a small drop of anhydrous MeOH added to keep the powder stable on the plate). The ACoF sample also showed a small amount of cobalt formate dihydrate impurity (3%) [Fig. S5, ESI†], while the ANiF and AMnF samples did not show evidence of any impurities [Fig. S3 and S4, ESI†].

High-pressure SCXRD

High-pressure single-crystal X-ray diffraction on AMFs were measured at the ID15B beamline at the European Synchrotron Radiation Facility, Grenoble, up to 2.4 GPa using monochromatic X-ray radiation (λ = 0.41112 Å) at ambient temperature. Membrane driven LeToullec type diamond anvil cells (DACs) were used, equipped with Boehler-Almax anvils. Stainless steel was used as the gasket material, and Daphne 7373 oil was used as the pressure-transmitting medium (in order to keep the same PTM as the magnetisation measurements). The solidification pressure of the Daphne oil is at 2.2–2.4 GPa,[59,60] and thus our diffraction experiments are within the hydrostatic regime of the PTM. Diffraction patterns were collected with a Mar555 flat panel detector using steps of 0.5° oscillations over a total ω scan range of 76° around the vertical axis. The pressures were measured using the ruby fluorescence method before and after each diffraction measurement. The average of both pressure values was used and the variance was employed to calculate errors associated with the pressure measurement. High-pressure single-crystal X-ray diffraction on AFeF was additionally measured at PETRA III, DESY, Hamburg, at the beamline P02.2 at 2.78 GPa using monochromatic X-ray radiation (λ = 0.2903 Å) with argon as the pressure-transmitting medium in order to resolve the high-pressure phase. We note that the use of neon as the PTM leads to the inclusion of Ne atoms into the AMF structures and changes the pressure-dependent behaviour.[61] Lattice parameter determination and integration of the reflection intensities were performed using the *CrysAlisPro* software.[62] Structure refinement was performed using SHELXL[63] within ShelXle[64] or JANA for the twinned data sets.[65]

A previous experiment on AFeF was conducted at the ID09A beamline at the European Synchrotron Radiation Facility, Grenoble (previous station of ID15B), up to 4.0 GPa using monochromatic X-ray radiation (λ = 0.411679 Å) at ambient temperature. The PTM used was argon, but the crystal quality wasn't good enough for single-crystal step scan collections and integrations. Instead wide image scans were collected ($\pm$20° rotation in 2 s exposure) and the extracted powder diffraction profile was refined to extract lattice parameters using Topas.[66]

Ambient-pressure SQUID measurements

Ambient pressure dc magnetisation measurements were carried out with a Quantum Design MPMS-5S SQUID equipped with a 5 T superconducting magnet and a continuous-flow cryostat. The samples AMnF, AFeF, ACoF, and ANiF were measured with zero-field cooling and field cooling from 300 to 2 K using a field of 100 Oe for AFeF, ACoF, and ANiF and 1000 Oe for AMnF (due to the weaker signal) [Fig. S7–S10, ESI†]. The measurements indicate weakly ferromagnetic behaviour below 9.9–10.0 K, 10.2 K, and 29.3 K for AFeF, ACoF and ANiF, respectively, determined from the intercept of two straight line fits before and after the change in slope. These values are close, although slightly overestimated, to the critical temperatures previously reported: 9.4 K, 9.8 K, and 29.3–29.5 K, for AFeF, ACoF and ANiF, respectively.[15,40] Purely antiferromagnetic order is observed for AMnF, with the T_N determined at 8.9 K from two straight line fits as described above (reported T_N at 8–8.4 K).[15,40] A small discontinuity in the magnetisation data can be observed for AFeF at 5 K, and for ACoF at 6 K. A similar discontinuity was reported in ACoF, $[(CH_3)_2NH_2][Co(HCOO)_3]$, and $[(CH_3)_2NH_2][Ni(HCOO)_3]$ at 6 K, 13 K, and 14 K respectively,[40,67] and the origin is thought to be due to a spin-reorientation transition, also observed in Muon spin relaxation measurements of $[(CH_3)_2NH_2][M(HCOO)_3]$ compounds.[68] It is also possible that the iron formate dihydrate impurity could give rise to the discontinuity observed in AFeF as it is close to the magnetic transition of iron formate dihydrate (3.8 K)[69] [Fig. S7, ESI†]. In addition, the first sample of AFeF exhibits a broad bump around 15 K [Fig. S7(a), ESI†], for this reason, the second sample of AFeF was employed for the high-pressure SQUID experiments [Fig. S7(b), ESI†].

High-pressure SQUID measurements

Pressure-dependent magnetic susceptibility data were measured in a miniature high-pressure cell of CuBe equipped with ceramic anvils and a CuBe gasket during field cooling.[70,71] Polycrystallites of AMnF (0.4 mg), AFeF (0.35 mg), ACoF (0.4 mg), or ANiF (0.3 mg) were loaded in the cell with Daphne 7373 oil as the pressure-transmitting medium. One small piece of lead

(~0.1 mg) was placed together with the sample inside the pressure cell and another lead piece was placed outside the pressure cell to serve as a pressure sensor. The pressure values at low temperature were determined by the difference between the superconducting transition temperatures between the two lead samples.[72] We note that a single superconducting transition was observed from both the lead inside and outside the cell at ambient pressure at the expected superconducting transition temperature, thus confirming the absence of a thermal gradient within the pressure cell. The empty cell background data measured at ambient pressure was subtracted from the ambient- and high-pressure SQUID measurements using an automatic background subtraction procedure.[70,73] We note that the deformation of the CuBe gasket upon compression does not significantly affect the magnetisation background due to its low contribution to the magnetisation.[70] Measurements of the lead and the sample were performed using a field of 20 Oe and 100 Oe, respectively for the AFeF, ACoF, and ANiF samples, and using a field of 1000 Oe for the AMnF sample. A higher field was used in the case of AMnF due to its low signal at p = 0 GPa. All samples were cooled to 2 K, apart from ANiF that was cooled to 7 K due to the large interference of the diamagnetic signal from the superconducting lead below this temperature.

DFT calculations

Exchange couplings and magnetic ground states were assessed using density-functional (DFT) band-structure calculations performed in the VASP code[74,75] using Perdew–Burke–Ernzerhof version of the exchange–correlation potential.[76] The mean-field DFT+U scheme was adapted in order to account for strong correlation effects for transition-metal d-orbitals. The on-site Coulomb repulsion parameter U_d was adjusted for each compound to match the observed J values as mentioned in the main text, whereas the Hund's exchange J_d was set to 1 eV for all transition metals, because it shows only a small variation across the 3d family.[77] The k-mesh with 64 points in the symmetry-irreducible part was used.

For the relaxation of the structures, the lattice parameters were kept fixed, whereas all atomic positions (including hydrogen positions) were optimized within DFT+U with residual forces below 0.005 eV Å^{-1}. We employed ferromagnetic order as it does not break the unit cell symmetry (unlike AFM order) and cross-checked that the magnetic order imposed during the relaxation has no significant influence on the optimized structures. As a test, we additionally applied AFM order on one structural model (AFeF-II) and observed that the exchange parameter and canted moment changed by less than 5%, so the choice of the spin configuration for the structure relaxation has no significant influence on the conclusions given in this work. Such relaxed structures were used for the calculation of magnetic couplings and the assessment of the magnetic ground state. In the case of the ambient $P6_322$ AMnF and ANiF variable-pressure structures, they were simplified to a $P6_3$ model with a ferroelectric arrangement of the ammonium cations (all NH_4 cations pointing in the same direction along the c-axis), allowing the same unit cell to be used as the ones obtained upon compression at ambient temperature. This model provides a simplification to the actual supercell that is created upon the ferroelectric transition but only affects the hydrogen bonding to the framework, that should only weakly affect the resulting magnetic properties (as no magnetoelectric coupling has been reported for this family of materials).

Model susceptibility curves for cubic antiferromagnets were obtained from quantum Monte-Carlo simulations performed in the loop code[78] of the ALPS package [Fig. S15–S17, ESI†].[79] Finite $L \times L \times L$ lattices with $L \leq 10$ were used to eliminate finite-size effects within the temperature range of the fitting.

Conflicts of interest

There are no conflicts to declare.

Acknowledgements

I. E. C. would like to acknowledge the Alexander von Humboldt Foundation for funding at the University of Bayreuth and the ESRF for financial support and provision of beamtime within the in-house research projects of the ID15B beamline. We acknowledge PETRA III light source at DESY for beamtime on the P02.2 beamline. I. E. C. thanks T. Boffa Ballaran for the use of the powder X-ray diffractometer, and N. Collings and A. L. Goodwin for useful discussions. N. D. thanks the DFG for financial support through the Heisenberg Program and Project No. DU 954-8/1. N. D. and L. D. gratefully acknowledge the Federal Ministry of Education and Research (BMBF, Germany) for funding. A. A. T. was funded by the Federal Ministry of Education and Research through the Sofja Kovalevskaya Award of Alexander von Humboldt Foundation.

References

1 G. Rogez, N. Viart and M. Drillon, *Angew. Chem., Int. Ed.*, 2010, **49**, 1921–1923.
2 Y. Tian, A. Stroppa, Y. Chai, L. Yan, S. Wang, P. Barone, S. Picozzi and Y. Sun, *Sci. Rep.*, 2014, **4**, 6062.
3 Y. Tian, A. Stroppa, Y.-S. Chai, P. Barone, M. Perez-Mato, S. Picozzi and Y. Sun, *Phys. Status Solidi RRL*, 2015, **9**, 62–67.
4 L. C. Gómez-Aguirre, B. Pato-Doldán, J. Mira, S. Castro-Garca, M. A. Señarís-Rodríguez, M. Sánchez-Andújar, J. Singleton and V. S. Zapf, *J. Am. Chem. Soc.*, 2015, **138**, 1122–1125.
5 A. Stroppa, P. Barone, P. Jain, J. M. Perez-Mato and S. Picozzi, *Adv. Mater.*, 2013, **25**, 2284–2290.
6 A. Stroppa, P. Jain, P. Barone, M. Marsman, J. M. Perez-Mato, A. K. Cheetham, H. W. Kroto and S. Picozzi, *Angew. Chem., Int. Ed.*, 2011, **50**, 5847–5850.
7 Z.-M. Wang, Y.-J. Zhang, T. Liu, M. Kurmoo and S. Gao, *Adv. Funct. Mater.*, 2007, **17**, 1523–1536.
8 P. Dechambenoit and J. R. Long, *Chem. Soc. Rev.*, 2011, **40**, 3249–3265.

9 O. Sato, T. Iyoda, A. Fujishima and K. Hashimoto, *Science*, 1996, **272**, 704–705.
10 O. Sato, J. Tao and Y.-Z. Zhang, *Angew. Chem., Int. Ed.*, 2007, **46**, 2152–2187.
11 K. Awaga, T. Sekine, M. Okawa, W. Fujita, S. M. Holmes and G. S. Girolami, *Chem. Phys. Lett.*, 1998, **293**, 352–356.
12 M. Ohba, W. Kaneko, S. Kitagawa, T. Maeda and M. Mito, *J. Am. Chem. Soc.*, 2008, **130**, 4475–4484.
13 W. Kaneko, M. Mito, S. Kitagawa and M. Ohba, *Chem. – Eur. J.*, 2008, **14**, 3481–3489.
14 W. W. Shum, J.-H. Her, P. W. Stephens, Y. Lee and J. S. Miller, *Adv. Mater.*, 2007, **19**, 2910–2913.
15 G.-C. Xu, W. Zhang, X.-M. Ma, Y.-H. Chen, L. Zhang, H.-L. Cai, Z.-M. Wang, R.-G. Xiong and S. Gao, *J. Am. Chem. Soc.*, 2011, **133**, 14948–14951.
16 J. M. Lawler, P. Manuel, A. L. Thompson and P. J. Saines, *Dalton Trans.*, 2015, **44**, 11613–11620.
17 Z. Wang, B. Zhang, Y. Zhang, M. Kurmoo, T. Liu, S. Gao and H. Kobayashi, *Polyhedron*, 2007, **26**, 2207–2215.
18 J.-P. Zhao, B.-W. Hu, F. Lloret, J. Tao, Q. Yang, X.-F. Zhang and X.-H. Bu, *Inorg. Chem.*, 2010, **49**, 10390–10399.
19 J.-P. Zhao, S.-D. Han, R. Zhao, Q. Yang, Z. Chang and X.-H. Bu, *Inorg. Chem.*, 2013, **52**, 2862–2869.
20 M. Mączka, A. Gągor, K. Hermanowicz, A. Sieradzki, L. Macalik and A. Pikul, *J. Solid State Chem.*, 2016, **237**, 150–158.
21 M. Wriedt and H.-C. Zhou, *Dalton Trans.*, 2012, **41**, 4207–4216.
22 M. Atzori, S. Benmansour, G. Mínguez Espallargas, M. Clemente-León, A. Abhervé, P. Gómez-Claramunt, E. Coronado, F. Artizzu, E. Sessini, P. Deplano, A. Serpe, M. L. Mercuri and C. J. Gómez García, *Inorg. Chem.*, 2013, **52**, 10031–10040.
23 D. Armentano, T. F. Mastropietro, G. De Munno, P. Rossi, F. Lloret and M. Julve, *Inorg. Chem.*, 2008, **47**, 3772–3786.
24 J. A. Navarro, E. Barea, A. Rodríguez-Diéguez, J. M. Salas, C. O. Ania, J. B. Parra, N. Masciocchi, S. Galli and A. Sironi, *J. Am. Chem. Soc.*, 2008, **130**, 3978–3984.
25 X.-H. Zhao, X.-C. Huang, S.-L. Zhang, D. Shao, H.-Y. Wei and X.-Y. Wang, *J. Am. Chem. Soc.*, 2013, **135**, 16006–16009.
26 P. W. Anderson, *Phys. Rev.*, 1959, **115**, 2–13.
27 J. Kanamori, *J. Phys. Chem. Solids*, 1959, **10**, 87–98.
28 J. B. Goodenough, *Magnetism and the Chemical Bond*, John Wiley & Sons, New York, 1963.
29 W. R. Entley, C. R. Treadway and G. S. Girolami, *Mol. Cryst. Liq. Cryst.*, 1995, **273**, 153–166.
30 S. M. Holmes and G. S. Girolami, *J. Am. Chem. Soc.*, 1999, **121**, 5593–5594.
31 R.-Y. Li, B.-W. Wang, X.-Y. Wang, X.-T. Wang, Z.-M. Wang and S. Gao, *Inorg. Chem.*, 2009, **48**, 7174–7180.
32 J. H. Song, K. S. Lim, D. W. Ryu, S. W. Yoon, B. J. Suh and C. S. Hong, *Inorg. Chem.*, 2014, **53**, 7936–7940.
33 J. Larionova, O. Kahn, J. Bartolome, R. Burriel, M. Castro, V. Ksenofontov and P. Gütlich, *Chem. Mater.*, 1999, **11**, 3400–3405.
34 C. H. Woodall, G. A. Craig, A. Prescimone, M. Misek, J. Cano, J. Faus, M. R. Probert, S. Parsons, S. Moggach, J. Martínez-Lillo, M. Murrie, K. V. Kamenev and E. K. Brechin, *Nat. Commun.*, 2016, **7**, 13870–13876.
35 M. Zentková, Z. Arnold, J. Kamarád, V. Kavečanský, M. Lukáčová, S. Mat'aš, M. Mihalik, Z. Mitróová and A. Zentko, *J. Phys.: Condens. Matter*, 2007, **19**, 266217.
36 D. Bloch, *J. Phys. Chem. Solids*, 1966, **27**, 881–885.
37 M. Drillon, P. Panissod, P. Rabu, J. Souletie, V. Ksenofontov and P. Gütlich, *Phys. Rev. B*, 2002, **65**, 104404.
38 C. J. Nuttall, T. Takenobu, Y. Iwasa and M. Kurmoo, *Mol. Cryst. Liq. Cryst.*, 2000, **343**, 227–234.
39 G.-C. Xu, X.-M. Ma, L. Zhang, Z.-M. Wang and S. Gao, *J. Am. Chem. Soc.*, 2010, **132**, 9588–9590.
40 Z. Wang, B. Zhang, K. Inoue, H. Fujiwara, T. Otsuka, H. Kobayashi and M. Kurmoo, *Inorg. Chem.*, 2007, **46**, 437–445.
41 Z. Wang, K. Hu, S. Gao and H. Kobayashi, *Adv. Mater.*, 2010, **22**, 1526–1533.
42 K.-L. Hu, M. Kurmoo, Z. Wang and S. Gao, *Chem. – Eur. J.*, 2009, **15**, 12050–12064.
43 P. Jain, V. Ramachandran, R. J. Clark, H. D. Zhou, B. H. Toby, N. S. Dalal, H. W. Kroto and A. K. Cheetham, *J. Am. Chem. Soc.*, 2009, **131**, 13625–13627.
44 X.-Y. Wang, Z.-M. Wang and S. Gao, *Chem. Commun.*, 2008, 281–294.
45 H. C. Walker, H. D. Duncan, M. D. Le, D. A. Keen, D. J. Voneshen and A. E. Phillips, *Phys. Rev. B*, 2017, **96**, 094423.
46 B. Pato-Doldán, L. C. Gómez-Aguirre, A. P. Hansen, J. Mira, S. Castro-García, M. Sánchez-Andújar, M. A. Señarís-Rodríguez, V. S. Zapf and J. Singleton, *J. Mater. Chem. C*, 2016, **4**, 11164–11172.
47 I. Dzyaloshinsky, *J. Phys. Chem. Solids*, 1958, **4**, 241–255.
48 T. Moriya, *Phys. Rev.*, 1960, **120**, 91–98.
49 B. Pato-Doldán, M. Sánchez-Andújar, L. C. Gómez-Aguirre, S. Yáñez-Vilar, J. López-Beceiro, C. Gracia-Fernández, A. A. Haghighirad, F. Ritter, S. Castro-García and M. A. Señarís Rodríguez, *Phys. Chem. Chem. Phys.*, 2012, **14**, 8498–8501.
50 I. E. Collings, M. Bykov, E. Bykova, M. G. Tucker, S. Petitgirard, M. Hanfland, K. Glazyrin, S. van Smaalen, A. L. Goodwin, L. Dubrovinsky and N. Dubrovinskaia, *CrystEngComm*, 2016, **18**, 8849–8857.
51 L. Mazzuca, L. Cañadillas-Delgado, J. A. Rodríguez-Velamazán, O. Fabelo, M. Scarrozza, A. Stroppa, S. Picozzi, J.-P. Zhao, X.-H. Bu and J. Rodríguez-Carvajal, *Inorg. Chem.*, 2017, **56**, 197–207.
52 R. D. Shannon, *Acta Crystallogr., Sect. A*, 1976, **32**, 751–767.
53 M. Sánchez-Andújar, L. C. Gómez-Aguirre, B. P. Doldán, S. Yáñez-Vilar, R. Artiaga, A. L. Llamas-Saiz, R. S. Manna, F. Schnelle, M. Lang, F. Ritter, A. A. Haghighirad and M. A. Señarís-Rodríguez, *CrystEngComm*, 2014, **16**, 3558–3566.
54 R. S. Manna, private communication, 2017.
55 A. A. Tsirlin, *Phys. Rev. B*, 2014, **89**, 014405.
56 J. A. Navarro, E. Barea, J. M. Salas, N. Masciocchi, S. Galli and A. Sironi, *Inorg. Chem.*, 2007, **46**, 2988–2997.
57 B. H. Kim and B. I. Min, *New J. Phys.*, 2011, **13**, 073034.
58 E. Colacio, J. M. Domínguez-Vera, M. Ghazi, R. Kivekäs, M. Klinga and J. M. Moreno, *Eur. J. Inorg. Chem.*, 1999, 441–445.
59 K. Yokogawa, K. Murata, H. Yoshino and S. Aoyama, *Jpn. J. Appl. Phys.*, 2007, **46**, 3636–3639.

60 N. Tateiwa and Y. Haga, *Rev. Sci. Instrum.*, 2009, **80**, 123901.
61 I. E. Collings, E. Bykova, M. Bykov, S. Petitgirard, M. Hanfland, D. Paliwoda, L. Dubrovinsky and N. Dubrovinskaia, *ChemPhysChem*, 2016, **17**, 3369–3372.
62 Rigaku Oxford Diffraction, *CrysAlisPro Software system, version 1.171.38.46*, Rigaku Corporation, Oxford, UK, 2018.
63 G. M. Sheldrick, *Acta Crystallogr., Sect. A*, 2007, **64**, 112–122.
64 C. B. Hübschle, G. M. Sheldrick and B. Dittrich, *J. Appl. Crystallogr.*, 2011, **44**, 1281–1284.
65 V. Petříček, M. Dušek and L. Palatinus, *Z. Kristallogr.*, 2014, **229**, 345–352.
66 A. A. Coelho, *TOPAS-Academic, version 4.1 (computer software)*, Coelho Software, Brisbane.
67 X.-Y. Wang, L. Gan, S.-W. Zhang and S. Gao, *Inorg. Chem.*, 2004, **43**, 4615–4625.
68 P. Baker, T. Lancaster, I. Franke, W. Hayes, S. Blundell, F. Pratt, P. Jain, Z.-M. Wang and M. Kurmoo, *Phys. Rev. B*, 2010, **82**, 012407.
69 P. Burlet, P. Burlet, J. Rossat-Mignod, A. de Combarieu and E. Bedin, *Phys. Status Solidi B*, 1975, **71**, 675–685.
70 N. Tateiwa, Y. Haga, Z. Fisk and Y. Ōnuki, *Rev. Sci. Instrum.*, 2011, **82**, 053906.
71 N. Tateiwa, Y. Haga, T. D. Matsuda, Z. Fisk, S. Ikeda and H. Kobayashi, *Rev. Sci. Instrum.*, 2013, **84**, 046105.
72 B. Bireckoven and J. Wittig, *J. Phys. E: Sci. Instrum.*, 1988, **21**, 841.
73 http://www.qdusa.com/sitedocs/appNotes/mpms/1014-213.pdf.
74 G. Kresse and J. Furthmüller, *Comput. Mater. Sci.*, 1996, **6**, 15–50.
75 G. Kresse and J. Furthmüller, *Phys. Rev. B*, 1996, **54**, 11169–11186.
76 J. P. Perdew, K. Burke and M. Ernzerhof, *Phys. Rev. Lett.*, 1996, **77**, 3865–3868.
77 V. I. Anisimov, J. Zaanen and O. K. Andersen, *Phys. Rev. B*, 1991, **44**, 943–954.
78 S. Todo and K. Kato, *Phys. Rev. Lett.*, 2001, **87**, 047203.
79 A. Albuquerque, F. Alet, P. Corboz, P. Dayal, A. Feiguin, S. Fuchs, L. Gamper, E. Gull, S. Gürtler, A. Honecker, R. Igarashi, M. Körner, A. Kozhevnikov, A. Läuchli, S. Manmana, M. Matsumoto, I. McCulloch, F. Michel, R. Noack, G. Pawłowski, L. Pollet, T. Pruschke, U. Schollwöck, S. Todo, S. Trebst, M. Troyer, P. Werner and S. Wessel, *J. Magn. Magn. Mater.*, 2007, **310**, 1187–1193.